metals

MDPI

Article

Thermodynamics and Agglomeration Behavior on Spinel Inclusion in Al-Deoxidized Steel Coupling with Mg Treatment

Lei Cao [1,2], Guocheng Wang [1,2,*], Xinghu Yuan [1,2], Pengliang Jin [1,2] and Seetharaman Sridhar [3]

[1] School of Materials and Metallurgy, University of Science and Technology Liaoning, Anshan 114051, China
[2] Key Laboratory of Chemical Metallurgy Engineering Liaoning Province, University of Science and Technology Liaoning, Anshan 114051, China
[3] Department of Metallurgical and Materials Engineering, Colorado School of Mines, Golden, CO 80401, USA
* Correspondence: wang_guocheng@163.com

Received: 22 July 2019; Accepted: 14 August 2019; Published: 16 August 2019



Abstract: There are many types of non-metallic $MgAl_2O_4$ inclusions observed in Al-deoxidized steel coupling with Mg treatment, including single-particle $MgAl_2O_4$, agglomerated $MgAl_2O_4$, and $MgAl_2O_4$-MnS. Thermodynamic calculation shows that $MgAl_2O_4$ precipitates in the liquid phase. The phase transformation follows liquid + Al_2O_3 + $MgAl_2O_4$ → liquid + $MgAl_2O_4$ → liquid + MgO + $MgAl_2O_4$ → liquid + MgO with the Mg content increasing when the Al content is a constant in molten steel, and it is in agreement with the experimental results for the formation of $MgAl_2O_4$ in molten steel. The calculation results of various attractive forces between two particles show that the cavity bridge force plays a dominant role in the agglomeration process and results in the agglomerated $MgAl_2O_4$. The lattice mismatch calculation result shows that $MgAl_2O_4$ can provide effective sites for MnS nucleating in steel.

Keywords: inclusion; thermodynamics; Al-deoxidization; Mg treatment; agglomeration mechanism

1. Introduction

Non-metallic inclusion has a great influence on the microstructure and performance of steel materials. Although many large-size inclusion particles can be removed into slag from molten steel in the steelmaking process, a small amount of inclusion with a wide size range remains unavoidable in steel products. In the process of steelmaking, aluminum is often used for deep deoxidation for liquid steel. However, solid alumina inclusions with a wide size range partially retained in the steel products destroy the microstructure and properties of the steel with their aggregation size and hard brittleness. Thus, controlling the chemistry, morphology, and size distribution of Al-deoxidation inclusion in steel is a key problem to improve the Al-killed steel performance.

Recently, magnesium is being widely used to disperse and refine inclusion, as it has strong agglomeration characteristics, such as Al_2O_3 particles in molten steel [1–6]. In those published works, after the magnesium addition, the large-sized and irregularly shaped Al_2O_3 inclusion in the steel were modified into small-sized and approximately spherical $MgAl_2O_4$ inclusion. Meanwhile, the average diameter of $MgAl_2O_4$ inclusion gradually decreases, while the number density of inclusion increases with the increase of magnesium content [7–9]. Yang [10] and Takata et al. [11] found that the total oxygen content drops to 15 ppm via Mg vapor deoxidation. The fine Mg-treated inclusion could be utilized to exert the "oxide metallurgy" to enhance the microstructures of steel products. However, some studies have found that fine $MgAl_2O_4$ inclusion particles after magnesium treatment partially agglomerate in the molten steel. The agglomeration of $MgAl_2O_4$ inclusions was also observed in our experiments. Wang et al. [7] and Du et al. [12] found that the attractive force of $MgAl_2O_4$ inclusion

has a certain relationship with inclusion radius by Newton's second law. Kimura et al. [13] thought that the aggregation of two $MgAl_2O_4$ particles based on the general expression of thermodynamic potential by the capillary force. However, a comparison of the effects of various attractive forces between $MgAl_2O_4$ particles leading to inclusion agglomeration in molten steel has not been reported. Therefore, we calculated various forces between $MgAl_2O_4$ particles in molten steel and determined the main factors. In addition, complex $MgAl_2O_4$-MnS inclusions were observed in the current experiment. Wen et al. [3], Li et al. [14], and Isobe et al. [15] used two-dimensional mismatch to calculate the lattice mismatch between $MgAl_2O_4$ between α-Fe, γ-Fe, and δ-Fe; however, a two-dimensional mismatch between $MgAl_2O_4$ and MnS has rarely been reported to explain the formation mechanism of $MgAl_2O_4$-MnS inclusions. We calculated the two-dimensional mismatch between $MgAl_2O_4$ and MnS to characterize the heterogeneous nucleation ability of MnS on $MgAl_2O_4$ inclusion.

The current work carried out a deoxidation for molten steel by Al coupling with Ni-Mg alloy and observed the two-dimensional (2D) and the three-dimensional (3D) morphologies of inclusions in the deoxidized solid steel samples. Based on these observations, the thermodynamics of Fe-Mg-Al-O melt were studied by FactSage, various attractive forces between $MgAl_2O_4$ particles in molten steel were calculated for clarifying the agglomeration of $MgAl_2O_4$ inclusion, and then the misfit degree between $MgAl_2O_4$ and MnS was calculated to reveal the formation mechanism of $MgAl_2O_4$-MnS inclusion.

2. Experimental

2.1. Materials and Processes

The compositions and quantities of experimental raw materials are as follows. Pure iron powder 500 g, ferrous oxalate 1.125 g (99 mass pct), Ni-Mg alloy 7.5 g, and the high purity aluminum 0.5 g (99.99 mass pct Al). The compositions of raw materials containing pure iron, Al wires, and Ni-Mg alloy are shown in Table 1.

Table 1. Chemical composition of raw materials (in mass percent, %).

Type	C	Si	Mn	P	S	Ni	Mg	Al
Pure Iron	<0.005	0.01	0.046	0.0032	0.013			
Ni-Mg alloy	0.012	0.001		0.002	0.0003	79.6747	20.31	
Al Wire								99.99

A tubular resistance furnace was used to smelt and deoxidize for molten steel. First, the pure iron powder and ferrous oxalate were placed into the alumina crucible (the oxygen content is almost 200 ppm in the melt) and then the alumina crucible was placed into the tubular resistance furnace. The temperature was raised to 1873 K (1600 °C) and held for 30 min to ensure complete melting of the pure iron in the crucible. Then, Al particles wrapped with high-purity iron were added into the melt, and then Ni-Mg alloy was immediately added into the melt. After 5 s, the molten steel was cooled down to room temperature in the furnace chamber at a rate of 4 K/min. The whole experimental process was protected by high-purity argon gas with an argon flow rate of 1 L/min.

2.2. Chemical Composition Analysis

The chemical compositions of the steel samples were analyzed by the chemical methods. The total oxygen T.O was measured using a nitrogen-oxygen analyzer (Model: TC600, LECO Corporation, St. Joseph, MI, USA). The total content of aluminum Al(t) was measured by the inductively coupled plasma-mass spectrometry (ICP-MS, Shimadzu Europa GmbH, Duisburg, Germany). The acid-soluble aluminum Al(s) content was measured by the chromazurol-s spectrophotometric method. The Mg content was measured by the inductively coupled plasma atomic emission spectrometry (ICP-AES, Spectro Analytical Instrument GmbH, Kleve, Germany).

2.3. Inclusion Samples Preparation

The solidified steel was cut into two semicircle steel samples (63 mm × 31.5 mm × 22 mm) as shown in Figure 1a by a wire electric discharge machine. Taking a rectangular sample (10 mm × 10 mm × 22 mm) from the center of the semicircles, as shown in Figure 1b,c. The rectangular sample was cut into two small rectangular samples, and the sample was polished by metallographic sandpaper with different particle sizes ranging from 60 mesh to 5000 mesh, and then the surface of the sample was polished to a mirror surface with surface area of 10 mm × 10 mm, as shown in Figure 1d.

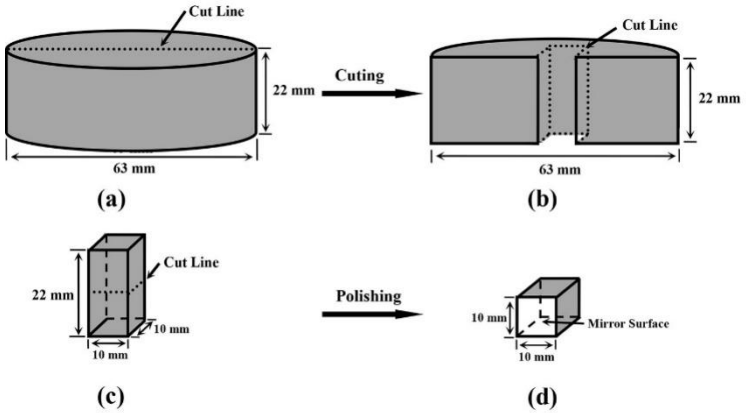


Figure 1. Samples preparation process. (**a**–**c**) Metallographic sample cutting process; (**d**) Metallographic sample polishing process.

The electrolysis set-up is shown in Figure 2. The steel sample as the anode, the copper plate as the cathode, and the electrolyte consists of 1 pct 4-methyl ammonium chloride, 5 pct tri-ethanolamine, 5 pct glycerol, and 89 pct methyl alcohol (in volume fraction). During the electrolysis process, the current density was controlled for 40 to 60 mA/cm^2 via a DC regulated power supply. The electrolyte was stirred with nitrogen gas to improve the kinetic conditions. After the electrolysis process, the sample was placed in ethanol for ultrasonic cleaning to obtain all particles. The carbide was separated by the ferromagnet from all particles in ethanol, and the residual inclusion particles were collected and placed on a double-sided conductive carbon tape for the electron microscope observation.

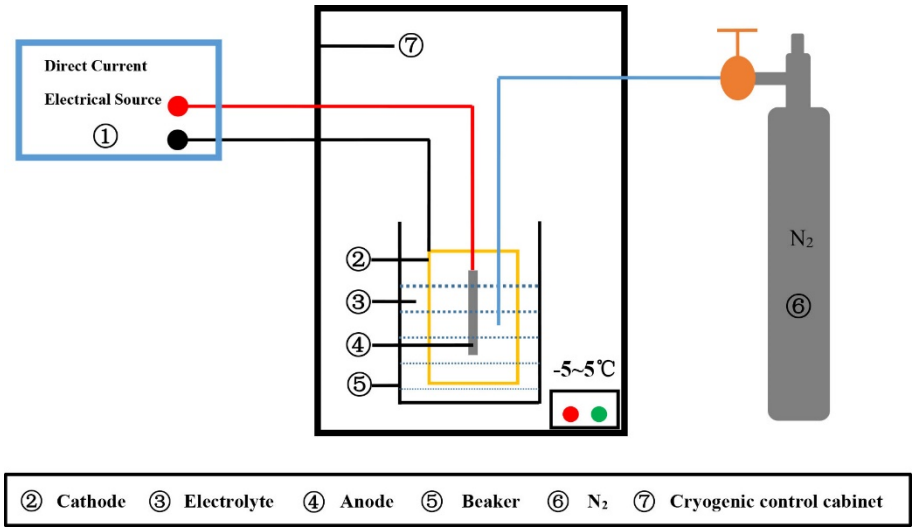


Figure 2. Electrolytic extraction device.

The samples prepared by the above two methods were placed in the field emission scanning electron microscope (FESEM, model: ZEISS ∑IGMA HD, Carl Zeiss, Oberkochen, Germany) for observation

and energy dispersive spectroscopy (EDS, model: Oxford-X-Max 50 mm^2, Carl Zeiss, Oberkochen, Germany) analysis.

3. Results

3.1. Experimental Steel Composition

Table 2 shows the chemical compositions of the experimental steel sample. The experimental steel can be considered as ultra-low-carbon steel. The silicon content is 30 ppm, which is lower than the production of general steel, the main source is raw materials and Ni-Mg alloys. The content of total Al ($Al_{(t)}$) is 0.003 mass percent higher than the content of acid-soluble Al ($Al_{(s)}$) in the steel sample. The content of Mg in the steel sample is 8 ppm. Since the surface of the molten steel is not covered with slag during the laboratory experiment, few inclusions leave the molten steel, so the total oxygen (T.O) content is 107 ppm.

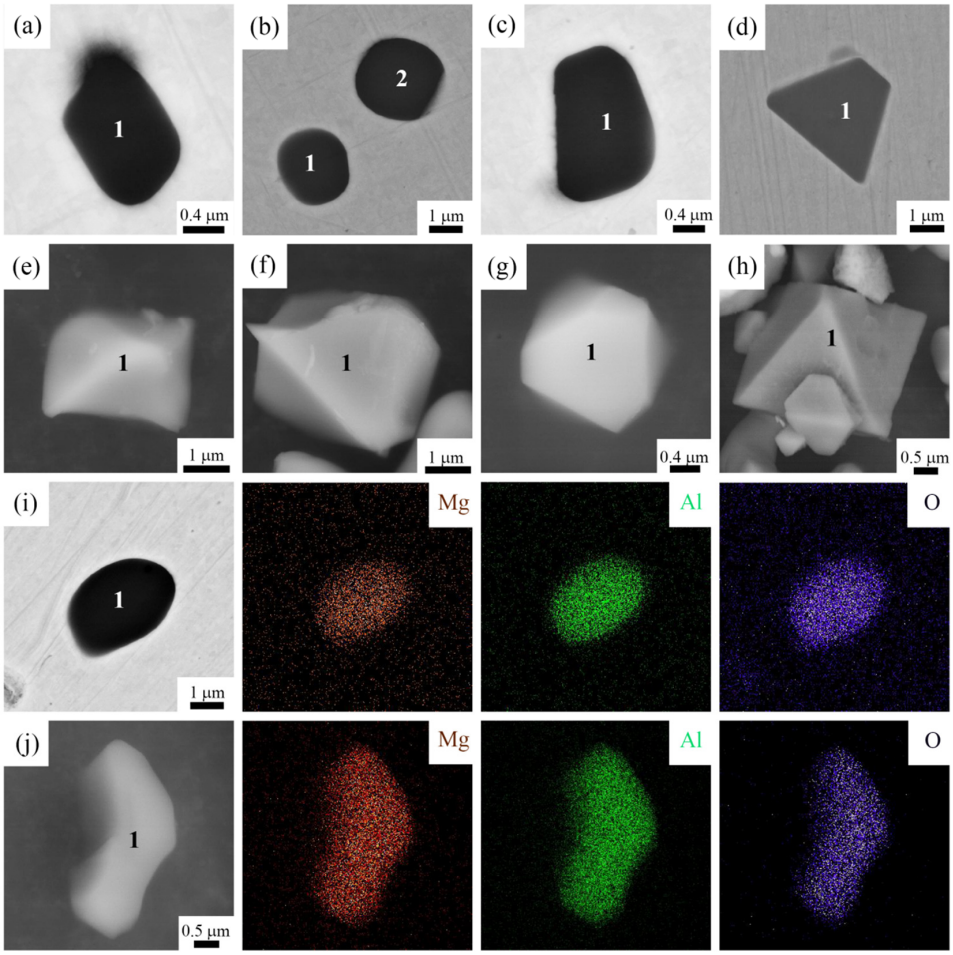
Table 2. Sample component test results (in mass percent, %).

Elements	C	Si	Mn	P	S	Al(s)	Al(t)	Mg	Ni	T.O
Content	0.0032	0.003	0.043	0.022	0.012	0.016	0.019	0.0008	0.955	0.0107

3.2. 2D and 3D Morphologies of Single and Aggregated $MgAl_2O_4$ Inclusions

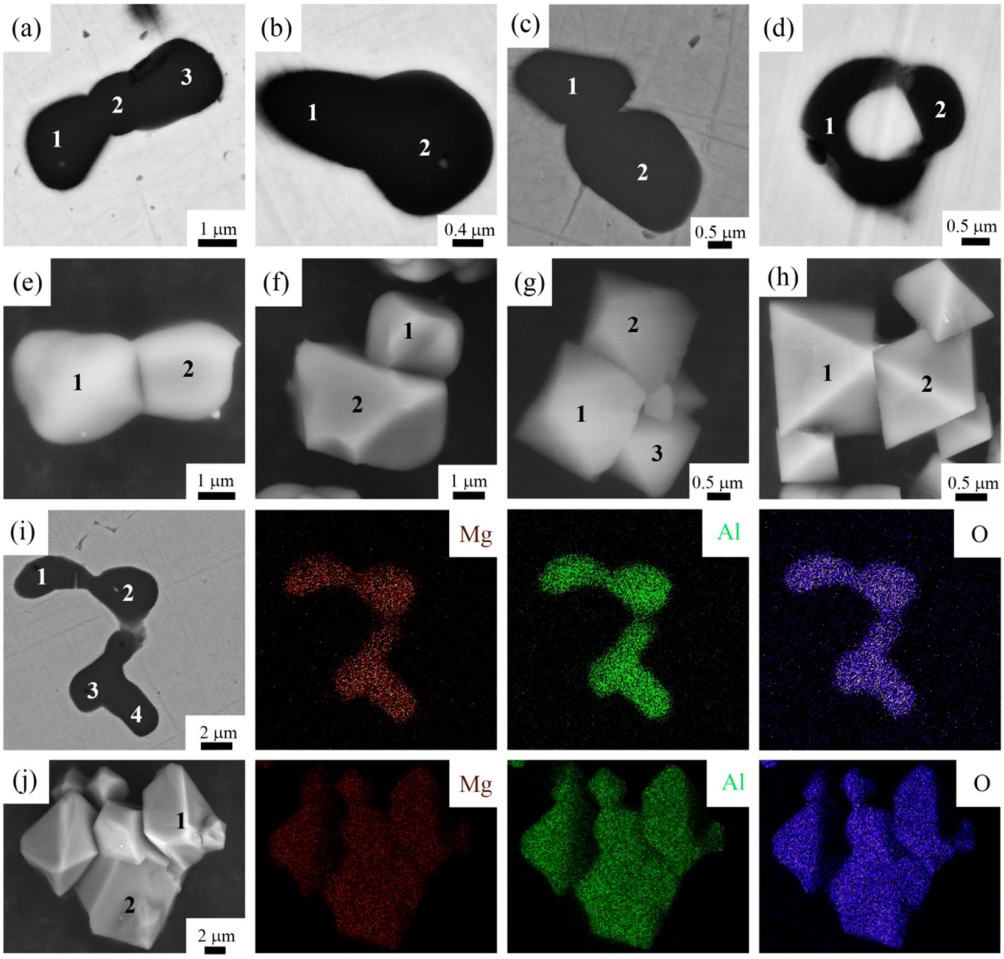
Figure 3 shows the 2D and 3D morphologies of single-particle $MgAl_2O_4$ inclusion by FESEM-EDS observation. Figure 3a–d shows the 2D morphologies of $MgAl_2O_4$ inclusion in the metallographic specimens, and these inclusion particles are long-strip, elliptical, and trapezoidal shape with a size of less than 4 μm in steel. Figure 3e–h shows the 3D morphologies of single-particle $MgAl_2O_4$ inclusion extracted from the steel specimens by the non-aqueous electrolysis method, and the 3D morphologies of $MgAl_2O_4$ inclusion particles are regular crystalline octahedron or approximate regular octahedron with a size range of 2–6 μm. Figure 3i–j shows the 2D and 3D morphologies and their elements mapping (Mg, Al, O) of $MgAl_2O_4$ inclusion and their shapes are dots and long-strip. Therefore, the 3D morphologies of $MgAl_2O_4$ inclusion indicate the obvious crystalline shape characteristics of $MgAl_2O_4$ spinel in steel that cannot be observed from their 2D morphologies.

Figure 4 shows the 2D and 3D morphologies of the aggregated $MgAl_2O_4$ inclusion in steel. Figure 4a–d shows the 2D morphologies of the aggregated $MgAl_2O_4$ inclusions with an elongated and annular shape, and the sizes of these $MgAl_2O_4$ inclusions are between 3 μm and 6 μm. Figure 4e–h shows the 3D morphologies of the aggregated $MgAl_2O_4$ inclusion with different shapes (long-strip and multi-particle stacking), whose sizes range from approximately 4 μm to 6 μm. The 3D morphologies display clearly the joints and inner interfaces of the aggregated $MgAl_2O_4$ inclusion and the contact patterns. Figure 4i,j show the 2D and 3D morphologies and element mapping (Mg, Al, O) of the agglomerated $MgAl_2O_4$ inclusion, and their shape is Z-shaped and multi-particle stacking. The aggregated $MgAl_2O_4$ inclusions are approximate 14 μm in Figure 4i and 21 μm in Figure 4j, respectively. It can be seen from the elements mapping figure that the aggregated $MgAl_2O_4$ inclusion are formed by the aggregation of several small-sized $MgAl_2O_4$ particles. It can be seen from the 3D morphologies that the contact interface between the two $MgAl_2O_4$ inclusion is very obvious. The contact between them is different from the phenomenon in which the reaction causes the aggregation of inclusions, which are bonded together by different surfaces of two $MgAl_2O_4$ inclusions. It can be found from the binding sites that the two $MgAl_2O_4$ inclusions are tightly packed and there is no trace of occurrence of breakage.



No.	EDS point analysis (at, %)		
	Mg	Al	O
(a)	10.94	23.82	65.34
(b)1	12.13	24.48	63.39
(b)2	12.28	24.23	63.49
(c)	11.38	23.75	64.87
(d)	12.47	23.81	63.72
(e)	11.90	22.58	65.52
(f)	13.52	25.86	60.62
(g)	12.60	25.18	62.22
(h)	15.93	31.04	53.03
(i)	9.41	24.50	66.10
(j)	10.18	23.16	66.66

Figure 3. 2D and 3D morphologies of single-particle $MgAl_2O_4$ inclusion. (**a**,**c**) Long-strip $MgAl_2O_4$; (**b**) Ellipsoidal $MgAl_2O_4$; (**d**) Trapezoidal $MgAl_2O_4$; (**e**–**h**) Regular crystalline octahedron $MgAl_2O_4$; (**i**,**j**) are dots and long-strip $MgAl_2O_4$ with elements mapping.

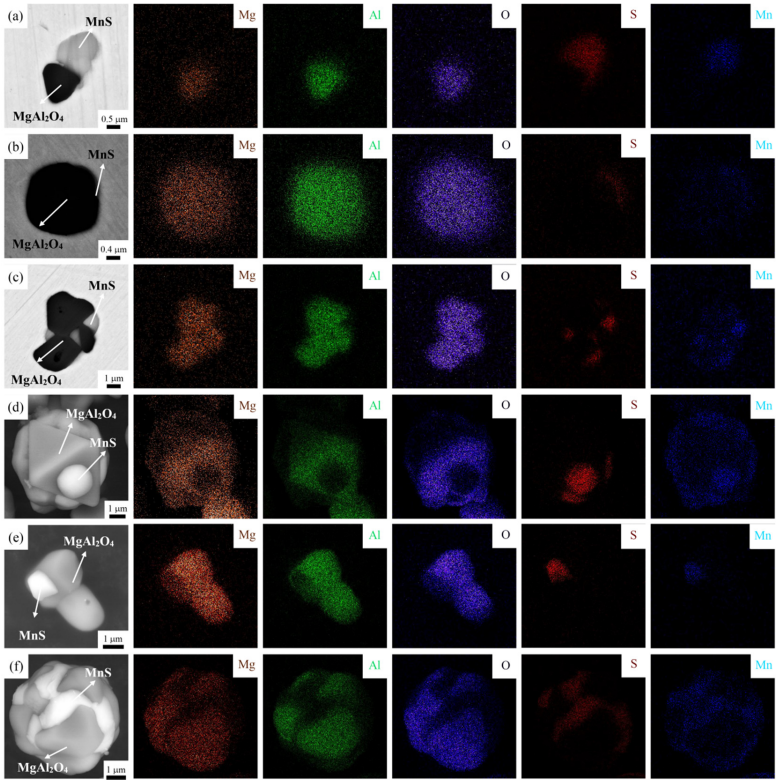


No.		EDS point analysis (at, %)			No.		EDS point analysis (at, %)		
		Mg	Al	O			Mg	Al	O
(a)	1	13.02	24.35	62.63	(g)	1	12.77	27.40	59.83
	2	13.65	24.77	61.58		2	12.47	25.23	62.30
	3	13.19	25.06	61.75		3	13.62	25.58	60.80
(b)	1	11.36	24.10	64.54	(h)	1	11.96	24.32	63.72
	2	12.12	24.27	63.61		2	11.81	24.26	63.93
(c)	1	12.02	23.81	64.17	(i)	1	11.33	23.63	65.04
	2	13.04	24.39	62.57		2	11.71	25.17	63.12
(d)	1	10.61	22.67	66.72		3	11.37	24.77	63.86
	2	11.31	23.35	65.34		4	12.05	25.94	62.01
(e)	1	12.09	22.76	65.15	(j)	1	11.71	22.28	66.01
	2	12.06	23.28	64.66		2	11.54	21.24	67.22
(f)	1	12.34	23.55	64.11					
	2	13.99	26.93	59.08					

Figure 4. 2D and 3D morphology of the aggregated $MgAl_2O_4$ inclusion. (**a**–**c**) Long-strip $MgAl_2O_4$; (**d**) Annular $MgAl_2O_4$; (**e**,**f**) Long-strip $MgAl_2O_4$; (**g**,**h**) Multi-particle $MgAl_2O_4$; (**i**) "Z" shape $MgAl_2O_4$ with elements mapping; (**j**) Multi-particle $MgAl_2O_4$ with elements mapping.

3.3. 2D and 3D Morphologies of $MgAl_2O_4$-MnS Inclusion

Figure 5 shows the 2D and 3D morphologies and elemental mappings of $MgAl_2O_4$-MnS inclusion in steel. Figure 5a–c shows the 2D morphologies of $MgAl_2O_4$-MnS inclusion and their elemental mappings. Figure 5a,b show the 2D morphologies of MnS embedded into the surface of the single-particle $MgAl_2O_4$ inclusion with the size of 3 μm, their shapes are upper and lower structure and spherical, while the inclusion in Figure 5c is MnS embedded into the multiple locations on the surface of the aggregated $MgAl_2O_4$ inclusion with the size of 5 μm. Figure 5d–f shows the 3D morphologies of $MgAl_2O_4$-MnS inclusion and their elemental mappings. Figure 5d shows that the MnS is embedded into the surface of a single-particle octahedral $MgAl_2O_4$ inclusion with the size of 4 μm, the shape is regular octahedron $MgAl_2O_4$ with MnS. Figure 5e,f show the MnS is embedded into the surface of aggregated $MgAl_2O_4$ inclusion. The inclusion is long-strip and ellipsoidal with dimensions of 5 μm in Figure 5e and 6 μm in Figure 5f, respectively. It can be seen from the surface elemental mapping that MnS is embedded into multiple locations on the surface of the aggregated $MgAl_2O_4$ inclusion.



No.	EDS point analysis (at, %)				
	Mg	**Al**	**O**	**Mn**	**S**
(a)	11.34	24.09	64.57	37.19	62.81
(b)	12.80	24.36	62.84	42.89	57.11
(c)	11.90	24.96	63.14	40.60	59.40
(d)	13.91	25.68	60.41	38.36	61.64
(e)	12.17	23.97	63.86	39.41	60.59
(f)	11.49	23.29	65.22	29.94	70.06

Figure 5. 2D, 3D morphologies, and elements mappings of $MgAl_2O_4$-MnS composite inclusion. (**a**) Upper and lower structure $MgAl_2O_4$-MnS; (**b**) Spherical $MgAl_2O_4$-MnS; (**c**) Multi-particle $MgAl_2O_4$-MnS; (**d**) Regular octahedron $MgAl_2O_4$ with MnS; (**e**) Long-strip $MgAl_2O_4$-MnS; (**f**) Ellipsoidal $MgAl_2O_4$-MnS.

4. Discussion

4.1. Thermodynamics of the Formation of $MgAl_2O_4$ Inclusion

The liquidus temperature and solidus temperature of the experimental steel were calculated to be 1807 K (1534 °C) and 1805 K (1532 °C) using Equations (1) and (2) [16], respectively.

$$\begin{aligned} T_{\mathrm{l}} = \quad & 1536 + 273 - \{78\,[\text{pct C}] + 7.6\,[\text{pct Si}] + 4.9\,[\text{pct Mn}] \\ & -34.3\,[\text{pct P}] - 38\,[\text{pct S}] + 3.6\,[\text{pct Al}]\} \end{aligned} \tag{1}$$

$$\begin{aligned} T_{\mathrm{s}} = \quad & 1536 + 273 - \{184.3\,[\text{pct C}] + 40.8\,[\text{pct Si}] + 8.6\,[\text{pct Mn}] \\ & +76.7\,[\text{pct P}] + 7.6.7\,[\text{pct S}] + 7.8\,[\text{pct Al}]\} \end{aligned} \tag{2}$$

Because the experiment is carried out by adding Mg alloy immediately after adding Al, the chemical reactions for the formation of $MgAl_2O_4$ can be expressed by Equation (3):

$$[\mathrm{Mg}] + 2[\mathrm{Al}] + 4[\mathrm{O}] = \mathrm{MgAl_2O_{4(s)}} \tag{3}$$

$$\log K^{\mathrm{E}}_{\mathrm{MgAl_2O_4}} = \frac{84339}{T} - 23.75 \tag{4}$$

$$K^{\mathrm{E}}_{\mathrm{MgAl_2O_4}} = \frac{a_{(\mathrm{MgAl_2O_4})}}{a_{(\mathrm{Mg})} \cdot {a_{(\mathrm{Al})}}^2 \cdot {a_{(\mathrm{O})}}^4} = \frac{a_{(\mathrm{MgAl_2O_4})}}{[\text{pct Mg}] f_{\mathrm{Mg}} \cdot ([\text{pct Al}]\, f_{\mathrm{Al}})^2 \cdot ([\text{pct O}]\, f_{\mathrm{O}})^4} \tag{5}$$

where $a_{(\mathrm{MgAl_2O_4})}$, $a_{(\mathrm{Mg})}$, $a_{(\mathrm{Al})}$, and $a_{(\mathrm{O})}$ denote the activity of $MgAl_2O_4$, Mg, Al, and O in molten steel, respectively; [pct Mg], [pct Al], and [pct O] represent the mass concentrations of Mg, Al, and O in the molten steel, respectively; f_{Mg}, f_{Al}, and f_{O} represent the activity coefficient of Mg, Al, and O in the molten steel, respectively.

When $a_{(\mathrm{MgAl_2O_4})} = 1$, both sides take the logarithm of 10 at the same time, and Equation (5) can be simplified to Equation (6):

$$\log K^{\mathrm{E}}_{\mathrm{MgAl_2O_4}} = -\log f_{\mathrm{Mg}} - 2\log f_{\mathrm{Al}} - 4\log f_{\mathrm{O}} - \log[\text{pctMg}] - 2\log[\text{pctAl}] - 4\log[\text{pctO}] \tag{6}$$

The iron content in molten steel is extremely high, and the second-order interaction coefficient is negligible. Combining Table 2 and the first-order interaction coefficient [17], the results are $\log f_{\mathrm{Mg}} = -5.997$, $\log f_{\mathrm{Al}} = -0.019$, $\log f_{\mathrm{O}} = -0.322$. Therefore, the formation temperature of $MgAl_2O_4$ inclusion is 1854 K (1581 °C).

The thermodynamic data and FactSage 7.2 software (ThermFact Inc., Montreal, QC., Canada) were used to calculate the effect of Mg on the transformation of Al_2O_3 inclusion phase in the Mg-Al-O-Fe melt system at 1873 K. The calculation results are shown in Figure 6. It can be seen from Figure 6 that when the Al content is a constant, as long as there is a trace amount of Mg, $MgAl_2O_4$ is formed. Al_2O_3 inclusion can gradually change into $MgAl_2O_4$ inclusion with the increasing of Mg content in the steel melt, all Al_2O_3 inclusion particles can be modified into $MgAl_2O_4$ inclusion. When the magnesium content reaches a certain value, the MgO phase is formed in the steel melt. With the further increase of magnesium content, the $MgAl_2O_4$ inclusion is changed into the MgO phase in molten steel. Many researchers [4,6,7,18–21] have studied magnesium-treated alumina inclusions with a concentration of magnesium in the range of 1–50 ppm, and the inclusions are Al_2O_3, MgO, and $MgAl_2O_4$. In this current study, the contents of Al, Mg, and O are 190 ppm, 8 ppm, and 107 ppm in the experimental steel sample (Table 2), respectively. The phases can be concluded to be the liquid phase, the $MgAl_2O_4$ spinel, and a small amount of Al_2O_3 phase in the experimental steel melt (the black point in Figure 6) at 1873 K. The thermodynamic analysis results are consistent with the experimental observation of the type of inclusions.

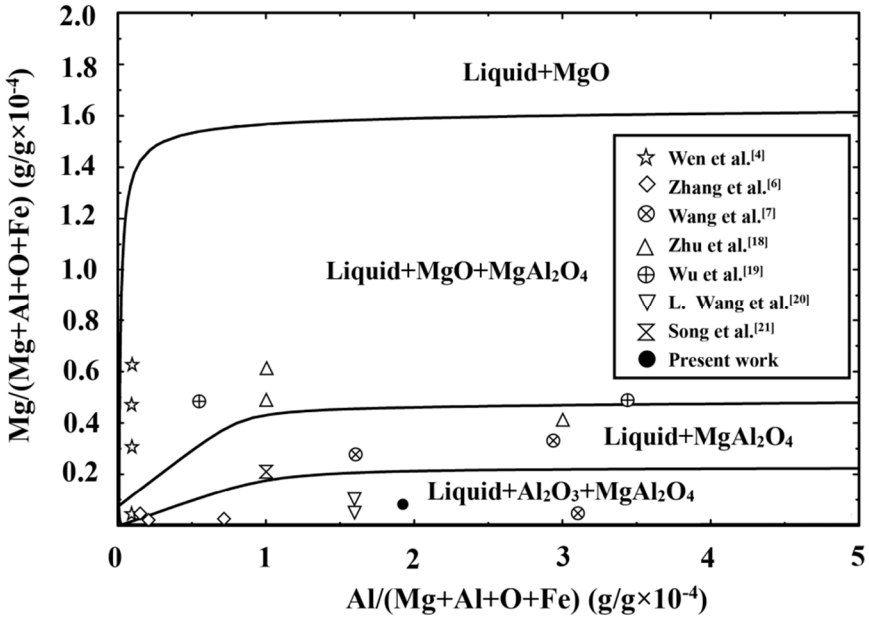


Figure 6. Stable structure phases of Mg-Al-O-Fe formation at 1873 K.

4.2. Mechanism on the Agglomeration of $MgAl_2O_4$ Inclusions

In this experiment, single particle octahedral $MgAl_2O_4$ and agglomerated $MgAl_2O_4$ were observed. In order to understand the aggregation mechanism of octahedral spinel particles, we calculated the van der Waals force, capillary force, and cavity bridge force that may occur between spinel particles. It is a regular octahedron model. Assuming that a regular octahedron has a side length of a, and the regular octahedron and the sphere have the same volume, then $d = \frac{a}{2} \cdot \mathrm{A}$ (A is a constant).

When two $MgAl_2O_4$ inclusion particles are close in molten steel, the van der Waals force for attraction can be expressed by Equation (7) [22]:

$$F_{\mathrm{V}} = [\mathrm{A}_{121}/(12 \cdot d^2)] \cdot \frac{a}{2} \tag{7}$$

where A_{121} represents the Hamaker constant of particles, 0.45×10^{-20}J [23]. a is assumed as 1 to 50 μm; In the calculation of this paper, A = 0.1, 0.14, 0.3. A = 0.14 is used in the literature [24], so this calculation covers this value. The calculation results of F_{V} are shown in Figure 7. As the side length of the two inclusions increases, the van der Waals force will gradually decrease. According to Paunov et al. [25], when two solid particles with poor wettability are close to each other in liquid steel, the surface of the molten steel is deformed, and then the capillary force is generated in a horizontal direction by two close $MgAl_2O_4$ inclusions in molten steel. The capillary force can be expressed by Equation (8):

$$F_{\mathrm{C}} = 2\pi \cdot \sigma_{\mathrm{Fe}} \cdot Q^2/(d + a) \tag{8}$$

where Q is the capillary charge (based on $\mathrm{J} = \mathrm{N} \cdot \mathrm{m}$, the unit of Q is m). σ_{Fe} [26] is the surface tension of molten steel, N/m. Since capillary charge has little dependence on the distance between surface particles, Q is approximately equivalent to Q_∞. The capillary charge between two solid particles, Q_∞ can be expressed by Equation (9) [27]:

$$Q_\infty = \frac{1}{6} q^2 \cdot \left(\frac{a}{2}\right)^3 \left(2 - 4\frac{\rho_{\mathrm{MgAl_2O_4}}}{\rho_{\mathrm{Fe}}} + 3\cos\theta - \cos^3\theta\right) \tag{9}$$

where q is the capillary constant, m^{-1}. q is expressed by $(\rho_{\mathrm{Fe}} \times g/\sigma_{\mathrm{Fe}})^{0.5}$. ρ_{Fe} represents the density of iron, 7000 kg/m^3 [28]. $\rho_{\mathrm{MgAl_2O_4}}$ represents the density of $MgAl_2O_4$ inclusion, 3578 kg/m^3 [28].

g represents the acceleration of gravity, 9.8 m/s^2. θ represents the angle between the inclusion of $MgAl_2O_4$ and the molten iron, 105° [29].

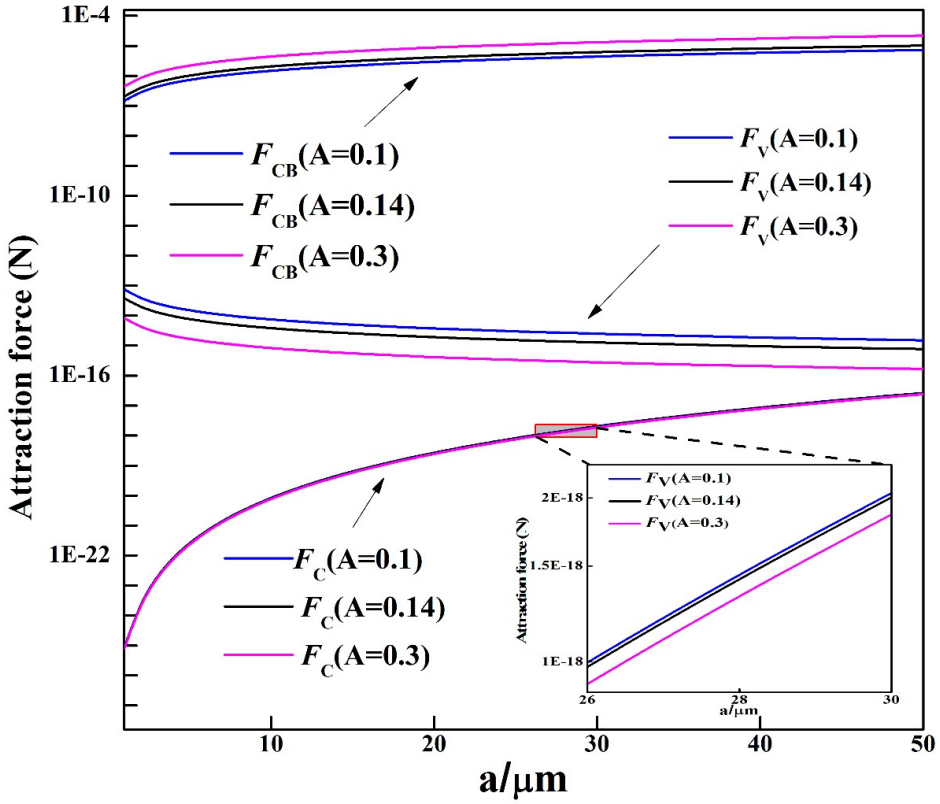


Figure 7. Relationship of van der Waals force, capillary force, cavity bridge force with particle side length.

The calculation result of F_C is shown in Figure 7. The capillary force between the two $MgAl_2O_4$ inclusion increases as the particle side length increases, but the F_C value is less than the van der Waals force. Furthermore, according to the theory of cavity bridges [24], for two unwetted inclusion particles in contact with molten steel, a cavity bridge is formed between the two particles when two $MgAl_2O_4$ inclusions are close together, as shown in Figure 8. As the radius of curvature of the cavity bridge is reduced, a cavity bridge force is generated. F_{CB} can be expressed by Equations (10) and (11) [24]:

$$F_{CB} = (1.54 - 1.88) \cdot d \cdot \sigma_{Fe} \tag{10}$$

$$\sigma_{Fe} = 2.858 - 0.00051T \tag{11}$$

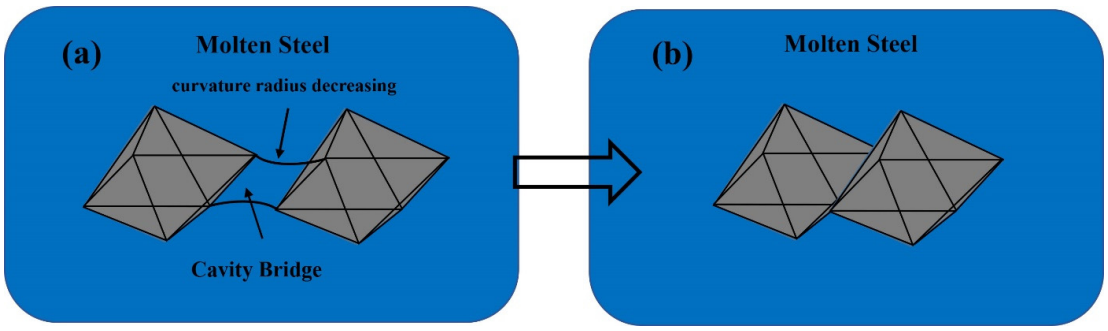


Figure 8. Schematic diagram of cavity bridge force. (**a**) Cavity bridge force formation process; (**b**) Aggregation of $MgAl_2O_4$ inclusion.

The calculation result of F_{CB} is shown in Figure 7. Comparing the calculated value of three attracting forces of F_V, F_C, and F_{CB}, it can be found that the cavity bridge could be the main force between two particles leading to inclusion aggregation, while the capillary force could be little affection for inclusion aggregation in the steel melt.

4.3. Mechanism on the Formation of $MgAl_2O_4$-MnS Inclusion

The $MgAl_2O_4$-MnS inclusion is a common complex inclusion in the current experimental steel. However, whether $MgAl_2O_4$ can be used as a MnS heterogeneous nucleation site is rarely reported. In this study, the equilibrium concentration product curve of MnS in molten steel was calculated according to Equations (12) and (13) [30].

$$MnS_{(s)} = [Mn] + [S] \tag{12}$$

$$\log K_{MnS} = \frac{a_{Mn} \cdot a_S}{a_{MnS}} = -\frac{6890}{T} + 4.16 \tag{13}$$

where a_{MnS}, a_{Mn}, a_S represent the activity of MnS, Mn, S, respectively.

The precipitation temperature of MnS is 1656 K (1383 °C), the liquidus temperature 1807 K (1534 °C) and solidus temperature 1805 K (1532 °C)

During the solidification process of the molten steel, it is assumed that the S element can diffuse completely. Therefore, the actual concentration of Mn and S can be obtained by Equations (14) and (15) [31]:

$$C_L^{Mn} = C_0^{Mn}(1 - f_s)^{k_{Mn}-1} \tag{14}$$

$$C_L^S = \frac{C_0^S}{1 - (1 - k_S)f_s} \tag{15}$$

where C_L^{Mn} and C_L^S represent the concentration of Mn and S at the solidification front, respectively; C_0^{Mn} and C_0^S denote the initial concentration of Mn, S in the molten steel, respectively; f_s is the solid fraction; k_{Mn} and k_S are the equilibrium distribution coefficients of Mn and S, respectively; k_{Mn} = 0.78 and k_S = 0.035 [32].

The actual concentration product Q_{MnS} during solidification can be expressed by Equation (16):

$$Q_{MnS} = C_L^{Mn} \cdot C_L^S = \frac{C_0^{Mn} \cdot C_0^S \cdot (1 - f_s)^{k_{Mn}-1}}{1 - (1 - k_S)f_s} \tag{16}$$

The relationship between the solid fraction and the temperature during solidification can be expressed by Equation (17) [16]:

$$T = T_0 - \frac{T_0 - T_1}{1 - f_s(T_1 - T_s)/(T_0 - T_s)} \tag{17}$$

where T is the temperature of the liquid phase during solidification. T_1 and T_s denote the liquidus temperature [1807 K (1534 °C)] and solidus temperature [1805 K (1532 °C)]. T_0 is the melting temperature of pure iron [1809 K (1536 °C)].

The relationship (log K_{MnS} and log Q_{MnS}) between the theoretical and actual concentration of MnS and the solidification fraction is calculated as shown in Figure 9. The equilibrium constant of MnS is equal to the theoretical concentration product of Mn and S (K_{MnS} = [pct Mn] × [pct S]), it can be calculated by Equation (13) and the actual concentration product Q_{MnS} is calculated by Equation (16), respectively. Precipitation of a solid phase will occur if the actual concentration reaches the equilibrium concentration (Q_{MnS} = K_{MnS}). There is no intersection point between log K_{MnS} and log Q_{MnS} in Figure 9. It indicates that the precipitation temperature of MnS is lower than the solidus temperature. $MgAl_2O_4$

precipitates in the liquid phase, and then $MgAl_2O_4$ inclusion can be wrapped by the MnS inclusion, forming the $MgAl_2O_4$-MnS inclusion.

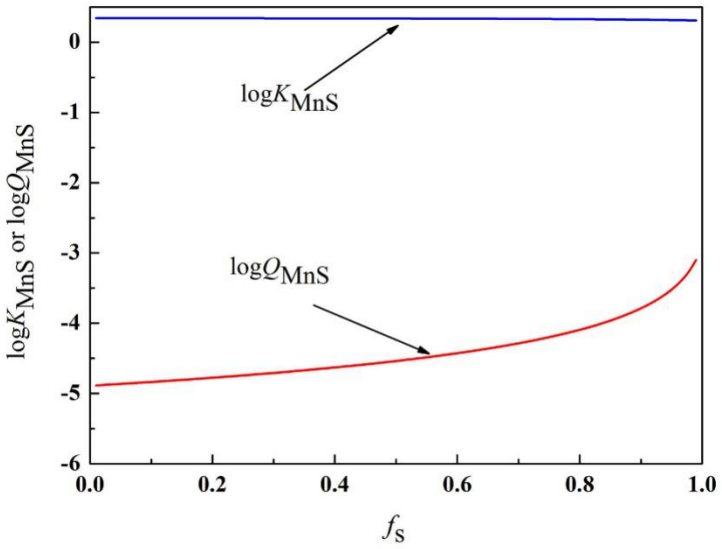


Figure 9. Relationship between the theoretical and actual concentration of MnS and the solidification fraction.

Figure 5 shows the MnS inclusions on the surface of $MgAl_2O_4$ inclusions. Both $MgAl_2O_4$ and MnS are cubic structures while MnS is a NaCl-type crystal, the mismatch occurs when MnS nucleates on the surface of $MgAl_2O_4$ since the atomic spacing between $MgAl_2O_4$ and MnS is different. The lattice parameters of $MgAl_2O_4$ and MnS are listed in Table 3 [33,34]. Bramfitt [35] proposed the lattice mismatch to characterize the ability of compound substrates to promote heterogeneous nucleation. The mismatch can be expressed by Equation (18):

$$\delta_{(hkl)_n}^{(hkl)_s} = \frac{1}{3}\left[\sum_{i=1}^{3}\frac{\left|d_{[uvw]_s}^{i}\cos\theta - d_{[uvw]_n}^{i}\right|}{d_{[uvw]_n}^{i}}\right]\times 100\% \quad (18)$$

where $(hkl)_s$ is a low-index crystal face on the substrate; $(uvw)_s$ is a low-index direction on the crystal plane $(hkl)_s$; $(hkl)_n$ is a low-index crystal plane on the nucleation phase; $(uvw)_n$ is a low-index direction on the $(hkl)_n$ crystal plane; $d[\mathrm{uvw}]_s$ is the spacing of atoms in the $(uvw)_s$ direction; $d[\mathrm{uvw}]_n$ is the spacing of atoms along the $(uvw)_n$ direction; θ is the angle between $(uvw)_s$ and $(uvw)_n$.

Table 3. Lattice parameter data for $MgAl_2O_4$ and MnS.

Inclusion	Crystal System	Lattice Parameter (nm)
$MgAl_2O_4$	Cubic	0.805 [33]
MnS	Cubic	0.524 [34]

Considering (110)MnS//(110)$MgAl_2O_4$ interface, (100)MnS//(100)$MgAl_2O_4$ interface and (111) MnS//(111)$MgAl_2O_4$ interface, the calculation results of the mismatch are shown in Table 4. The mismatch of (110)MnS//(110)$MgAl_2O_4$ and (100)MnS//(100)$MgAl_2O_4$interface is 7.94%, and it indicates that the lattice matching degree of $MgAl_2O_4$ and MnS is higher at (110) and (100) interface.

Table 4. Calculation results of lattice mismatch of $MgAl_2O_4$ and MnS.

Case	$[hkl]_s$	$[hkl]_n$	$d[hkl]_s$	$d[hkl]_n$	θ,deg	Mismatch (δ)
(110)MnS//(110)$MgAl_2O_4$	[–111]	[001]	7.41	8.05	-	-
	[001]	[–112]	9.076	9.859	0	7.94%
	[–110]	[–110]	5.24	5.692	-	-
(100)MnS//(100)$MgAl_2O_4$	[011]	[011]	5.24	5.692	-	-
	[010]	[010]	7.41	8.05	0	7.94%
	[01–1]	[01–1]	5.24	5.692	-	-
(111)MnS//(111)$MgAl_2O_4$	[–110]	[–110]	3.705	5.692	-	-
	[–12–1]	[–12–1]	6.418	9.859	0	38.60%
	[01–1]	[01–1]	3.705	5.692	-	-

5. Conclusions

(1) The Al-deoxidation coupling with Mg treated experiment has been carried out, the 3D morphologies of octahedral $MgAl_2O_4$, and agglomerated $MgAl_2O_4$, $MgAl_2O_4$-MnS inclusion particles were observed by non-aqueous electrolysis extraction method and FESEM.

(2) Thermodynamic calculation shows $MgAl_2O_4$ precipitates in the liquid phase. The phase transformation follows liquid + Al_2O_3 + $MgAl_2O_4$ → liquid + $MgAl_2O_4$ → liquid + MgO + $MgAl_2O_4$ → liquid + MgO with the Mg content increasing when the Al content is a constant in molten steel.

(3) The cavity bridge force acts as the dominant force leading to the agglomeration of two $MgAl_2O_4$ particles in the molten steel. Two $MgAl_2O_4$ inclusions can connect with each other due to the action of the cavity bridge force.

(4) Thermodynamic calculations show that the precipitation temperature of MnS inclusions is lower than the solidus temperature, so $MgAl_2O_4$-MnS inclusions can be formed. The mismatch degree of $MgAl_2O_4$-MnS interface indicates that $MgAl_2O_4$ inclusion can provide heterogeneous nucleation sites for MnS, while MnS can nucleate on (110) and (100) plane of $MgAl_2O_4$ inclusion easily.

Author Contributions: Methodology, G.W. and X.Y.; Project administration, G.W.; Writing-original draft preparation, L.C.; Writing-review and editing, L.C.; Reviewing, P.J. and S.S.

Funding: This research was funded by National Natural Science Foundation of China (Grant No. 51874170).

Acknowledgments: The authors are grateful to the National Natural Science Foundation of China (Grant No. 51874170) for supporting this work.

Conflicts of Interest: The authors declare no conflict of interest.

References

1. Min, Y.; Li, X.; Yu, Z.; Liu, C.; Jiang, M.F. Characterization of the acicular ferrite in Al-deoxidized low-carbon steel combined with Zr and Mg additions. *Steel Res Int.* **2016**, *87*, 1503–1510. [CrossRef]
2. Xie, J.; Zhang, D.; Yang, Q.; An, J.; Huang, Z.; Fu, J. Exploration of morphology evolution of the inclusions in Mg-treated 16MnCrS5 steel. *Ironmak. Steelmak.* **2018**, 1–10. [CrossRef]
3. Ma, W.; Bao, Y.; Wang, M.; Zhao, L. Effect of Mg and Ca treatment on behavior and particle size of inclusions in bearing steels. *ISIJ Int.* **2014**, *54*, 536–542. [CrossRef]
4. Wen, B.; Song, B.; Pan, N.; Hu, Q.; Mao, J. Effect of SiMg alloy on inclusions and microstructures of 16Mn steel. *Ironmak. Steelmak.* **2011**, *38*, 577–583. [CrossRef]
5. Chang, C.; Jung, I.; Park, S.C.; Kim, H.S.; Lee, H.G. Effect of Mg on the evolution of non-metallic inclusions in Mn-Si-Ti deoxidised steel during solidification:experiments and thermodynamic calculations. *Ironmak. Steelmak.* **2005**, *32*, 251–257. [CrossRef]
6. Zhang, T.S.; Liu, C.J.; Jiang, M.F. Effect of Mg on behavior and particle size of inclusions in Al-Ti deoxidized molten steels. *Metall. Mater. Trans. B* **2016**, *47B*, 2253–2262. [CrossRef]
7. Wang, H.; Li, J.; Shi, C.B.; Li, J. Evolution of Al_2O_3 inclusions by magnesium treatment in H13 hot work die steel. *Ironmak. Steelmak.* **2017**, *44*, 128–133. [CrossRef]

8. Jiang, Z.H.; Wang, C.; Gong, W.; Wang, H.D. Evolution of inclusions and change of as-cast microstructure with Mg addition in high carbon and high chromium die steel. *Ironmak. Steelmak.* **2015**, *42*, 669–674. [CrossRef]
9. Kim, H.S.; Chang, C.H.; Lee, H.G. Evolution of inclusions and resultant microstructural change with Mg addition in Mn/Si/Ti deoxidized steels. *Scripta Mater.* **2005**, *53*, 1253–1258. [CrossRef]
10. Yang, J.; Yamasaki, T.; Kuwabara, M. Behavior of inclusions in deoxidation process of molten steel with in situ produced Mg vapor. *ISIJ Int.* **2007**, *47*, 699–708. [CrossRef]
11. Takata, R.; Yang, J.; Kuwabara, M. Characteristics of inclusions generated during Al-Mg complex deoxidation of molten steel. *ISIJ Int.* **2007**, *47*, 1379–1386. [CrossRef]
12. Du, G.; Li, J.; Wang, Z.B.; Shi, C.B. Effect of magnesium addition on behavior of collision and agglomeration between solid inclusion particles on H13 steel melts. *Steel Res. Int.* **2017**, *88*, 1600185. [CrossRef]
13. Kimura, S.; Nakajima, K.; Mizoguchi, S. Behavior of alumina-magnesia complex inclusions and magnesia inclusions on the surface of molten low-carbon steels. *Metall. Mater. Trans. B* **2001**, *32B*, 79–85. [CrossRef]
14. Li, J.; Li, J.; Shi, C.B.; Wang, L.L.; Wu, Z.; Wang, H. Effect of trace magnesium on carbide improvement in H13 steel. *Can. Metall. Quart.* **2016**, *55*, 321–327. [CrossRef]
15. Isobe, K. Effect of Mg addition on solidification structure of low carbon steel. *ISIJ Int.* **2010**, *50*, 1972–1980. [CrossRef]
16. Chen, P.J.; Zhu, C.Y.; Li, G.Q.; Dong, Y.W.; Zhang, Z.C. Effect of sulphur concentration on precipitation behaviors of MnS-containing inclusions in GCr15 bearing steels after LF refining. *ISIJ Int.* **2017**, *57*, 1019–1028. [CrossRef]
17. Park, J.H.; Lee, S.B.; Gaye, H.R. Thermodynamics of the formation of MgO-Al_2O_3-TiOx inclusions in Ti-stabilized 11Cr ferritic stainless steel. *Metall. Mater. Trans. B* **2008**, *39B*, 853–861. [CrossRef]
18. Zhu, L.; Wang, Y.; Wang, S.; Zhang, Q.; Zhang, C. Research of microalloy elements to induce intragranular acicular ferrite in shipbuilding steel. *Ironmak. Steelmak.* **2019**, *46*, 499–507. [CrossRef]
19. Wu, Z.; Zheng, W.; Li, G.; Matsuura, H.; Tsukihashi, F. Effect of inclusions' behavior on the microstructure in Al-Ti deoxidized and magnesium-treated steel with different aluminum contents. *Metall. Mater. Trans. B* **2015**, *46*, 1226–1241. [CrossRef]
20. Wang, L.; Li, J.; Ning, B.; Li, Y. Effects of magnesium on wear resistance of H13 steel. *Mater. Trans.* **2014**, *55*, 1104–1108. [CrossRef]
21. Song, M.; Hu, C.; Song, B.; Zhu, H.; Xue, Z.; Xu, R. Effect of Ti-Mg treatment on the impact toughness of heat affected zone in 0.15% C-1.31% Mn steel. *Steel Res. Int.* **2018**, *89*, 1700355. [CrossRef]
22. Taniguchi, S.; Kikuchi, A. Mechanisms of collision and coagulation between fine particles in fluid. *Tetsu-to-Hagané* **1992**, *78*, 527–535. [CrossRef]
23. Visser, J. On hamaker constants: A comparison between hamaker constants and lifshitz-van der Waals constants. *Adv. Colloid Interface Sci.* **1972**, *3*, 331–363. [CrossRef]
24. Sasai, K. Interaction between alumina inclusions in molten steel due to cavity bridge force. *ISIJ Int.* **2016**, *56*, 1013–1022. [CrossRef]
25. Paunov, V.N.; Kralchevsky, P.A.; Denkov, N.D.; Nagayama, K. Lateral capillary forces between floating submillimeter particles. *J. Colloid Interface Sci.* **1993**, *157*, 100–112. [CrossRef]
26. Poirier, D.R.; Yin, H.B.; Suzuki, M.; Emi, T. Interfacial Properties of Dilute Fe-O-S Melts on Alumina Substrates. *ISIJ Int.* **1998**, *38*, 229–238. [CrossRef]
27. Chan, D.Y.C.; Henry, H.J.D., Jr.; White, L.R. The interaction of colloidal particles collected at fluid interfaces. *J. Colloid Interf. Sci.* **1981**, *79*, 410–418. [CrossRef]
28. Mu, W.Z.; Dogan, N.; Coley, K.S. Agglomeration of non-metallic inclusions at the steel/Ar interface: Model Application. *Mater. Trans. B* **2017**, *48B*, 2092–2103. [CrossRef]
29. Wang, L.Z.; Yang, S.F.; Li, J.S.; Zhang, S.; Ju, J.T. Effect of Mg addition on the refinement and homogenized distribution of inclusions in steel with different Al contents. *Metall. Mater. Trans. B* **2017**, *48B*, 805–818. [CrossRef]
30. Kim, W.Y.; Jo, J.O.; Chung, T.I.; Kim, D.S.; Pak, J.J. Thermodynamics of titanium, nitrogen and TiN formation in liquid iron. *ISIJ Int.* **2007**, *47*, 1082–1089. [CrossRef]
31. Liu, Y.; Zhang, L.F.; Duan, H.J.; Zhang, Y.; Luo, Y.; Conejo, A.N. Extraction, thermodynamic analysis, and precipitation mechanism of MnS-TiN complex inclusions in low-sulfur steels. *Metall. Mater. Trans. A* **2016**, *47A*, 3015–3025. [CrossRef]
32. Luo, S.; Wang, B.Y.; Wang, Z.H.; Jiang, D.B.; Wang, W.L.; Zhu, M.Y. Morphology of solidification structure and MnS inclusion in high carbon steel continuously cast bloom. *ISIJ Int.* **2017**, *57*, 2000–2009. [CrossRef]

33. Passerini, L. Ricerche sugli spinelli.-II. I composti. $CuAl_2O_4$, $MgAl_2O_4$, Mg Fe_2O_4, $ZnAl_2O_4$, $ZnCr_2O_4$, Zn Fe_2O_4, $MnFe_2O_4$. *Gazz. Chim. Ital.* **1930**, *60*, 389–399.
34. Ott, H. Die strukturen von MnO, MnS, AgF, NiS, SnJ_4, SrCk, BaF_2. *Z. Krist.- Cryst. Mater.* **1926**, *63*, 222–230. [CrossRef]
35. Bramfiti, B.L. The effect of carbide and nitride additions on the heterogeneous nucleation behavior of liquid iron. *Metall. Trans.* **1970**, *1*, 1987–1995. [CrossRef]



© 2019 by the authors. Licensee MDPI, Basel, Switzerland. This article is an open access article distributed under the terms and conditions of the Creative Commons Attribution (CC BY) license (http://creativecommons.org/licenses/by/4.0/).